Fatigue of Cold-Work Tool Steels: Effect of Heat Treatment and Carbide Morphology on Fatigue Crack Formation, Life, and Fracture Surface Observations

KENZO FUKAURA, YOSHIHIKO YOKOYAMA, DAIEN YOKOI, NOBUHIRO TSUJII, and KANJI ONO

The fatigue properties of two types of cold-work tool steels tempered at various temperatures were evaluated. The microstructure and fracture surface morphology were correlated to the fatigue behavior. Cold-work tool steels using this study were a conventional tool steel (JIS SKD11; 1.4C-11Cr-0.8Mo-0.2V) and its modified steel (M-SKD11; 0.8C-8Cr-2Mo-0.5V). The fatigue strength of the M-SKD11 steel increased 20 pct over that of the SKD11 steel for any number of cycles. This is attributed to the refinement of primary M_7C_3 carbides. These M_7C_3 carbides fractured during fatigue and were found at the sites of fatigue crack initiation. Change in crack initiation behavior was confirmed by acoustic emission testing. The S–N curves of the steels are similar to those of most structural steels. However, the subsurface fatigue crack initiation was dominant at lower alternating stresses. This study points to a general approach of carbide refinement that can be used for the enhancement of fatigue properties.

I. INTRODUCTION

IN recent years, metal working dies have been subjected to more severe environment, because of the necessity of working with high-strength materials for the automobile and electronics industries.[1,2,3] Widespread use of near-net-shape processing requires the maintenance of close tolerances throughout the life of the dies. Consequently, the life of typical cold-work tool steels has been noticeably shortened.[4,5,6] Fatigue life was also reduced from an increasing number of stress concentration sites, from high die pressures, and from chipping due to impact loading.[7,8] Therefore, a strong need exists to develop low-cost tool steels with high strength and toughness as well as high resistance to fatigue.[9]

Numerous studies exist on fatigue properties of high-strength steels, such as high-speed tool steels, bearing steels, and cold-work tool steels. These generally show that nonmetallic inclusions initiate fatigue fracture.[8,10–15] However, studies on effects of carbides on fatigue behavior have been limited.[16,17,18] These reports suggest that fractured carbides or the debonding at the carbide-matrix interface can initiate fatigue, acting similarly to cracked inclusions. The roles of carbides should, thus, be explored in order to develop fatigue-resistant tool steels.

We have completed an alloy development project for an improved cold-work tool steel. The goals of this project were to increase the strength, toughness, wear resistance, and resistance to temper softening. The last characteristic is important since surface hardening treatments such as carbonitriding and ion-nitriding are applied on tool-steel dies.[4,19] The starting material of this work was JIS SKD11 with the composition of 1.4C-11.1Cr-0.80Mo-0.23V (equivalent to AISI D2). The composition was adjusted to reduce the amount of primary carbides with lower carbon and chromium, balancing this with higher molybdenum and vanadium to obtain higher secondary hardening effects. The optimized composition was 0.8C-8Cr-2Mo-0.5V. The lower C and Cr levels reduced the as-quenched martensite hardness and the size of the primary M_7C_3 carbide,[20] while higher Mo and V contributed to better secondary hardening and hardenability.[21] Because of reduced and refined primary carbides, fatigue behavior is expected to be enhanced.

The aim of this study is to examine the fatigue behavior of the newly developed tool steel in connection with its microstructure and to ascertain the origin of improvement through the S–N curve, acoustic emission, and fractographic analyses. Using the SKD11 tool steel as a reference material, we also want to clarify effects of carbide size distribution on fatigue behavior of the tool steels.

II. EXPERIMENT

Table I shows the chemical composition of steels used in this study: SKD11 and its modified version, to be referred to as M-SKD11. M-SKD11 contains lower C and lower Cr, but 2 to 2.5 times Mo and V. Alloys were air-melted in a 60-ton electric furnace, refined in a ladle furnace, vacuum-degassed in an RH furnace (Ruhrstahl-Heraeus process), and cast into ingots with 400 × 400 mm cross section. These were homogenized and hot rolled at 1398 K with a reduction ratio 268 and were annealed at 1143 K to spheroidize primary carbides. Tensile and fatigue test specimens were rough machined. The specimens were heated at 1303 K and air quenched. The quenched specimens were double tempered in the range of 473 to 873 K and held for 3.6 ks followed by air cooling for each of the double-tempering treatments. Specimens for fatigue testing were tempered at 473, 773, and 833 K for SKD11 and at 473, 793, and 833 K for M-SKD11. Fatigue specimens were also double tempered at each temperature and held for 3.5 ks. Specimens

---

KENZO FUKAURA, Professor, and YOSHIHIKO YOKOYAMA, Assistant Professor, are with the Department of Materials Science and Engineering, Hemeji Institute of Technology, Himeji 671-22, Japan. Contact e-mail: fukaura@mse.eng.himeji-tech.ac.jp DAIEN YOKOI, Research Engineer, is with the Research and Development Center, Sanyo Special Steel Co. Ltd., Himeji 672, Japan. NOBUHIRO TSUJII, formerly Research Engineer, is Head, High Alloy Steel Group, Technical Administration Department, Sanyo Special Steel Co. Ltd. KANJI ONO, Professor, is with the Department of Materials Science and Engineering, University of California, Los Angeles, CA 90095.

Manuscript submitted November 26, 2002.

with the geometry shown in Figure 1 were finish machined by grinding. After grinding, all specimens were carefully polished in the longitudinal direction by abrasive papers and a diamond polisher using 1-μm paste to obtain the smooth mirror finish.

Tensile tests were performed at an initial strain rate of 8.3×10^{-4} s^{-1}. Fully reversed, axial fatigue tests ($R = -1$) were performed using samples of Figure 1(b) with a servohydraulic testing machine under load control with the conditions of sine-wave excitation, 1 Hz frequency, and at ambient temperature. Using cylindrical specimens as shown in Figure 1(c), a clip gage was attached to measure the plastic strain during fatigue. The fracture surfaces after tensile and fatigue testing were examined using a scanning electron microscope (JSM-5200, JEOL*).

For metallurgical evaluation, an optical microscope and a transmission electron microscope were used, operating at an acceleration voltage of 200 kV (HF2000, Hitachi Ltd., Japan).

Table I. Chemical Composition of Cold-Work Tool Steels Used in This Study (Weight Percent)

Steels	C	Si	Mn	Cr	Mo	V	P	S
SKD11	1.41	0.24	0.41	11.10	0.80	0.23	0.023	0.001
M-SKD11	0.80	0.88	0.39	8.10	1.90	0.52	0.022	0.001

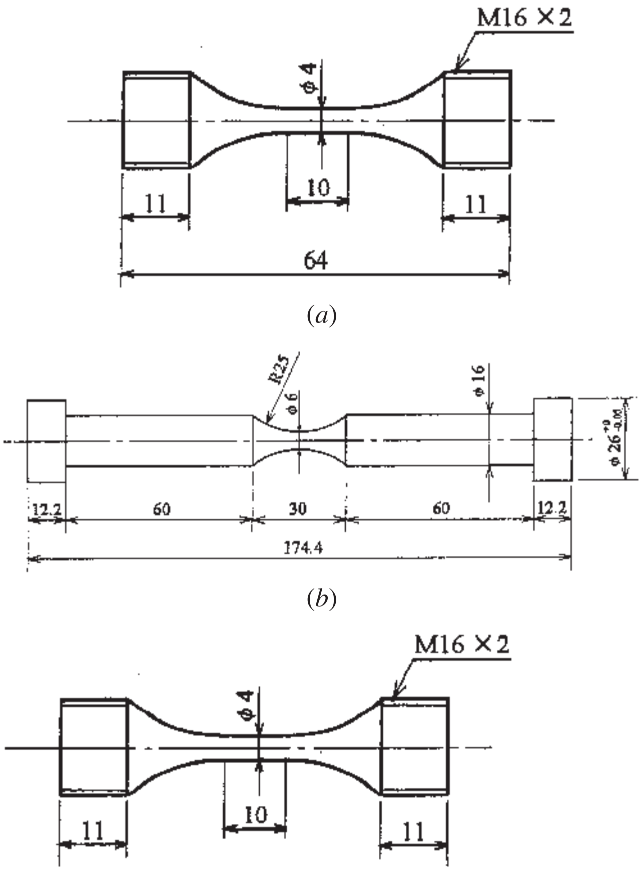

(*a*)

(*b*)

(*c*)

Fig. 1—Shape and size of (*a*) tensile specimen and (*b*) and (*c*) fatigue specimens. All dimensions in millimeters.

An etchant of 3 mL of nitric acid and 100 mL of methanol was used to reveal prior austenite grain boundaries. X-ray diffraction was used to identify carbides extracted electrolytically. The solution composition to extract carbides is 10 pct acetylacetone and 1 pct tetramethylammonium chloride in methanol. The normal electrode potential referred to that of hydrogen was -200 mV. To determine the chemical composition of the carbides, a wavelength dispersive X-ray microanalyzer (JXA8900R, JEOL) was used. The amount of retained austenite (γ) was measured by X-ray diffraction using (200)α' and (220)γ reflections, which have a relatively small degree of overlap with carbide diffraction peaks.[22,23]

Acoustic emission (AE) was monitored during tensile testing of the two steels. Two resonant sensors (MAC375, Acoustic Emission Technology Corp., CA, USA) were attached at both ends of the reduced section, and signal waveforms and AE parameters were recorded using two 2-channel data recording systems (Mistras 2001, Physical Acoustics Corp., NJ, USA). The AE signals due to carbide cracking or micro-cracking were discriminated from the noise using the arrival-time-difference read directly from the recorded AE signals. Further details are given in Reference 24.

III. RESULTS AND DISCUSSION

A. *Microstructural Characteristics and Tensile Properties*

Microstructures of steel samples were characterized with respect to their carbides, since the carbide morphology in hardened steel strongly influences the mechanical properties.[5,10,11] Figure 2 shows the optical micrographs of as-quenched SKD11 and M-SKD11 with prior austenite grain boundaries revealed and two types of particles delineated: massive white particles

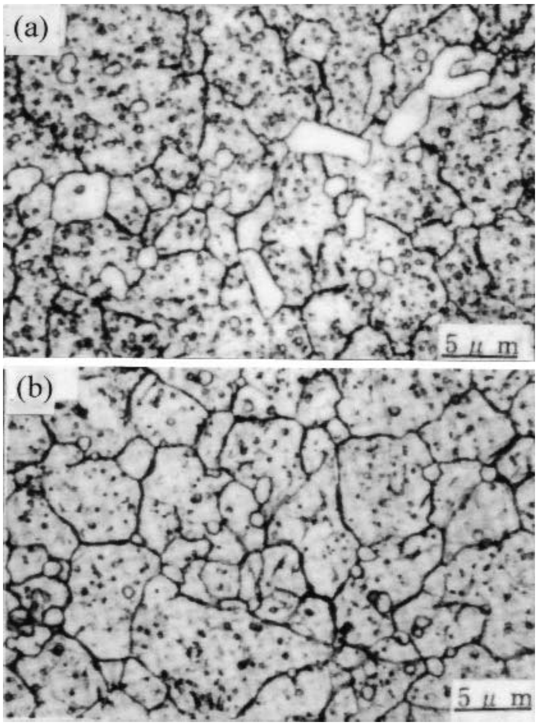

Fig. 2—Microstructures of (*a*) SKD11 and (*b*) M-SKD11.

---

*JEOL is a trademark of Japan Electron Optics Ltd., Tokyo.

Table II. Microstructural Characteristics for Both Tool Steels

Steels	Kind of Carbides	V_f of Carbides (Pct)	Mean Diameter of Carbides (μm)	Maximum Diameter of Carbides (μm)	Interparticle Distance between M_7C_3 Carbides (μm)	Prior Austenite Grain Size (μm)	Retained Austenite Volume Percent
SKD11	M_7C_3	7.5	5.3	21.5	3.1	5.3	20 (273 to 673 K)
	$M_{23}C_6$	6.0	0.6	—	3.1	5.3	7 (773 K) 0 (793 K)
M-SKD11	M_7C_3	2.2	2.5	14.4	5.3	6.9	13 (273 to 673 K)
	$M_{23}C_6$	2.3	0.5	—	5.3	6.9	8 (773 K) 4 (793 K) 0 (833 K)

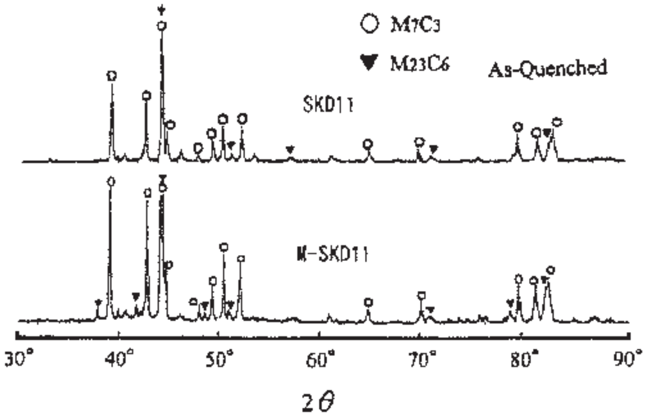

Fig. 3—X-ray diffraction patterns of electrolytically extracted carbide residue for SKD11 and M-SKD11.

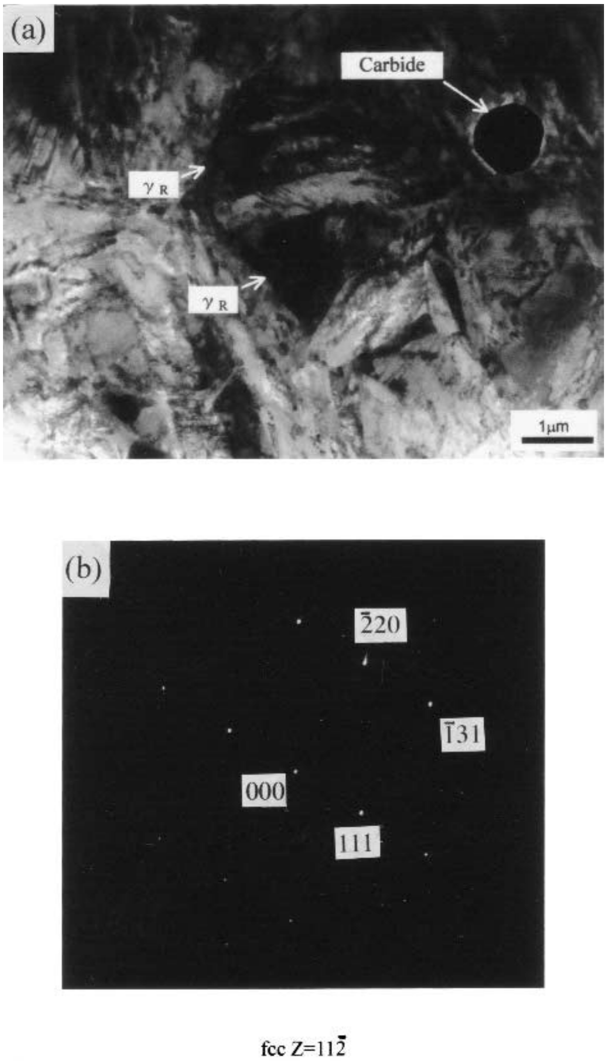

Fig. 4—(*a*) TEM micrograph of bright-field image and (*b*) selected area diffraction pattern from retained austenite for M-SKD11 tempered at 473 K.

and small black round particles. The massive carbide was identified using X-ray microanalysis as M_7C_3 and its chemical composition was (Fe_{28}, Cr_{37}, V_1, Mo_1)C_{33}. The chemical composition of submicron round particles could not be determined with certainty. The prior austenite grain size was 5.3 μm for SKD11 and 6.9 μm for M-SKD11. The white M_7C_3 particles in SKD11 were larger than those in M-SKD11.

In M-SKD11 steel, the carbides are smaller and tend to exist at grain-boundary triple points. Average size, volume fraction, and maximum size of these carbides were determined by using 100 optical micrographs taken at 1000 magnification. Each carbide particle was outlined before submitting the micrograph to an automatic image analyzer. The results are listed in Table II. When the particle size is smaller than about 1 μm, however, distinguishing the massive and round particles became difficult. The reported volume fraction results for the round particles (later identified as $M_{23}C_6$) appear to include some massive M_7C_3. Figure 3 shows X-ray diffraction patterns of electrolytically extracted residues. Both steels include numerous peaks corresponding to M_7C_3 and $M_{23}C_6$ carbides in the as-quenched state. The kind of carbides was not changed with tempering. Retained austenite content in the as-quenched state was 20 pct in SKD11 and 13 pct in M-SKD11. As shown in Figure 4, retained austenite phases exist mostly at the surroundings of carbides and were nearly unchanged with tempering up to 700 K. However, when tempered near 800 K, the retained austenite decomposed. These microstructural results are also listed in Table II.

The M-SKD11 steel has a relatively smaller carbide size and has a smaller amount of carbide because of its lower C and Cr contents. Interparticle spacing between carbides in M-SKD11 was large and the degree of M_7C_3 segregation was found to be smaller. The observed microstructural characteristics are consistent with the Fe-Cr-C phase diagrams shown in Figure 5.[25] The vertical dashed line in

Figure 5(a), which is the section at 8 pct Cr, corresponds to M-SKD11 and that in Figure 5(b) (12 pct Cr section) is for SKD11. Figure 5(b) indicates that primary M_7C_3 carbide exists at solidification in Fe-12Cr-1.4C, while the composition of the M-SKD11 passes through the austenite single-phase field before precipitating M_7C_3 carbide. Although the presence of Mo and V affects the phase diagrams, the primary eutectic carbides in SKD11 are expected to precipitate directly from the liquid phase. In the M-SKD11 steel, M_7C_3 carbides should separate from the austenite.[25] Thus, these are not strictly the primary carbides that were formed from the melt.

Table III shows Vickers hardness, tensile, and impact properties of the two steels, air-quenched from 1303 K and tempered at four different temperatures. The hardness of the as-quenched material is 865HV for SKD11 and 785HV for M-SKD11, and it initially decreases with increasing tempering temperature. However, both materials reach the peak secondary hardening in the temperature range of 773 to 793 K. The extent of secondary hardening in M-SKD11, which contains significantly more Mo and V, is larger than that in SKD11 and achieves a higher maximum hardness at 793 K. The tensile strength of tempered M-SKD11 is 20 to 30 pct greater at each temperature as well. It is noteworthy that the fracture

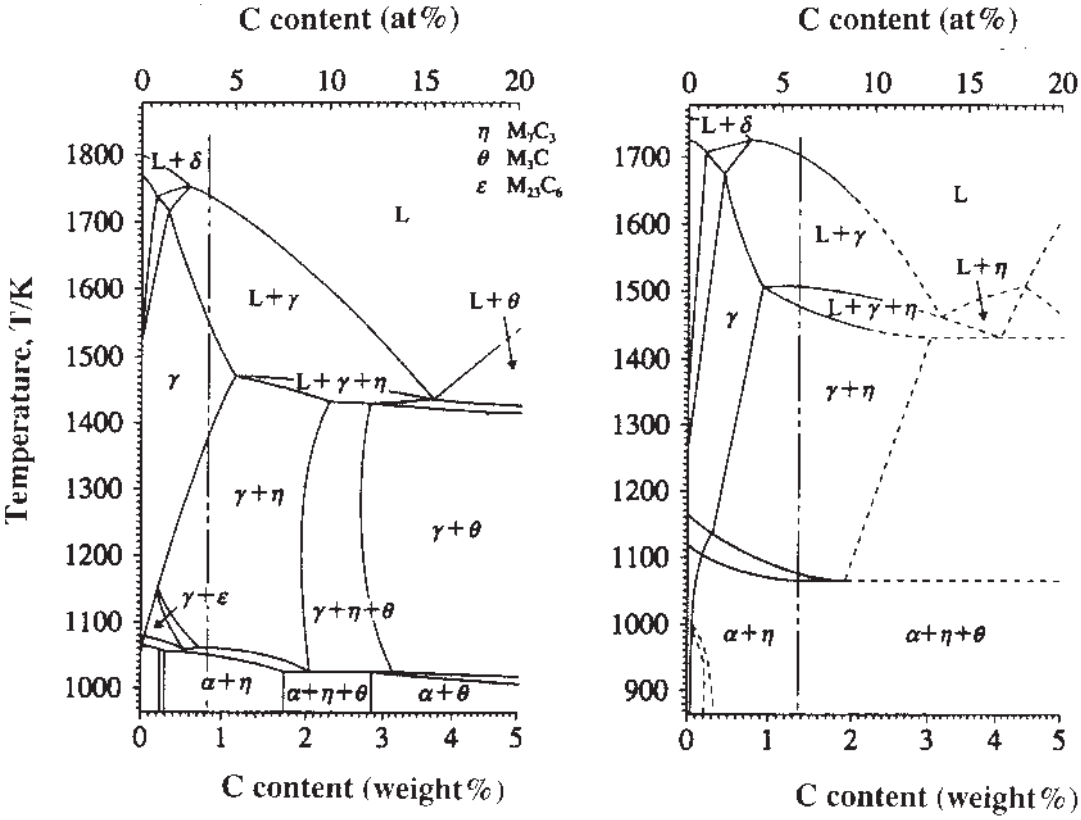

(a) 8 weight % Cr vertical section **(b) 12 weight % Cr vertical section**

Table III. Tensile and Impact Properties of Cold-Work Tool Steels

Steels	Tempering Temperature (K)	HV	0.2 Pct Offset Yield Strength (MPa)	Ultimate Tensile Strength (MPa)	Fracture Elongation (Pct)	Reduction in Area (Pct)	Work per Unit Volume* (J/m^3)	Charpy C-Notch Toughness (kJ/m^2)
SKD11	473	711	1360	1970	2.7	4.3	9.0×10^8	150
	673	642	1440	1960	1.8	4.6	8.6	150
	773	765	1660	2190	1.6	1.5	8.8	130
	833	603	1410	1790	2.3	5.9	9.9	270
M-SKD11	473	693	1580	2430	4.8	4.9	22.2	1200
	673	660	1750	2350	3.9	7.4	17.8	1170
	793	791	2040	2620	2.9	5.0	16.2	500
	833	683	1790	2350	4.0	10.8	19.5	1000

*Area under stress-strain curve.

elongation of M-SKD11 is 3 to 5 pct and is about twice that of SKD11. The ratio of the yield strength to tensile strength was 0.76 to 0.79 for both steels tempered to peak hardening, but was 0.65 to 0.69 for 473 K temper (no secondary hardening). The lower value appears to be a consequence of a high amount of retained austenite (20 pct for SKD11 and 13 pct for M-SKD11, as shown in Table II).

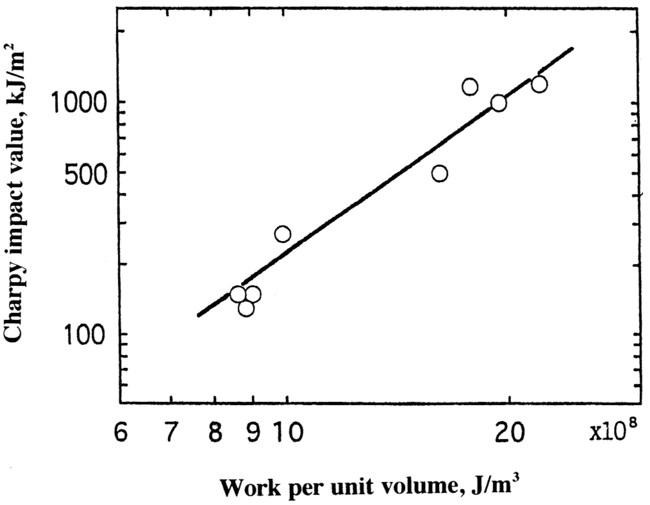

Fig. 6—Relationship between work per unit volume obtained by measuring the area under stress-strain curves and C-notch Charpy impact energy.

Table III also provides the data on plastic work (or the area under the stress-strain curves, sometimes considered to represent toughness[26]) and Charpy C-notch toughness. The latter is based on the round-notch geometry of a 10-mm radius and 2-mm depth on an otherwise standard Charpy specimen. (This notch shape is often adopted for the testing of high-hardness materials having over 55 in Rockwell C-scale.[27]) The C-notch toughness of M-SKD11 is about 5 times that of SKD11. The logarithmic relationship between Charpy impact value and the work per unit volume is shown in Figure 6. This indicates that Charpy C-notch toughness increases with the square of the plastic work. Although a conventional Charpy energy is sometimes related to fracture toughness,[26] the Charpy C-notch toughness used here represents the work of plastic deformation and the total volume of deformation under C-notch.

Figure 7 shows examples of the tensile fracture surfaces of tempered steels. Fracture is internally initiated and propagates radially. Particles are always found at the fracture initiation site, with dimples surrounding them. These particles were examined using an X-ray microanalyzer and most of them were identified as carbides: they were not debonded, but fractured. Another type of particle at the fracture initiation site is Al-Si-oxide, which is debonded by tensile loading.

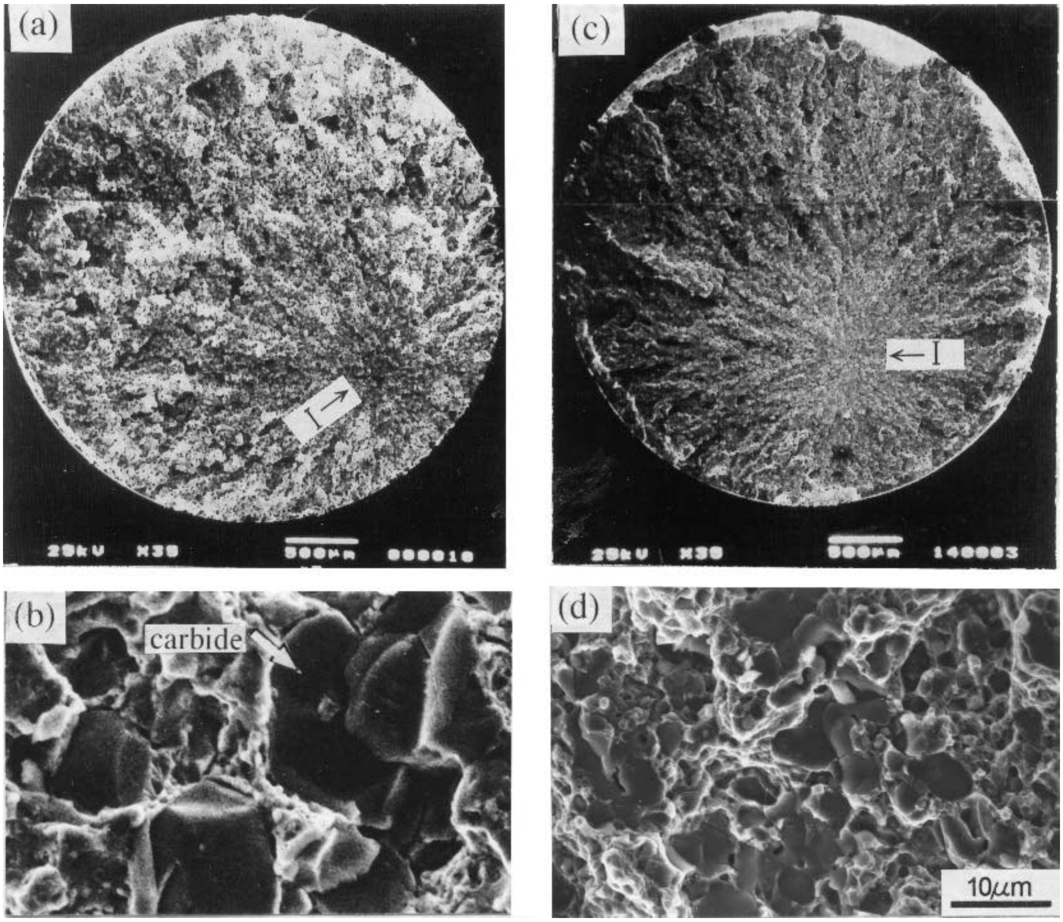

Fig. 7—Scanning electron micrographs of tensile fracture surfaces of (*a*) and (*b*) SKD11 and (*c*) and (*d*) M-SKD11, tempered at 573 K. (b) and (d) Magnified photographs of their fracture initiation sites.

B. *Fatigue Strength*

Figure 8 shows the S–N curves of materials tempered at 473 K, 773 or 793 K, and 833 K. The fatigue testing used hour-glass-shaped samples of Figure 1(b) and was conducted with $R = -1$ in a tension-compression mode. Two data points at 10^7 cycles represent unfractured M-SKD11 samples. Thus, the fatigue limit is expected to be higher than 750 MPa for M-SKD11. The S–N curve of each steel may be represented by a single straight line. However, data points for the secondary hardened specimens have a tendency to locate upward of the S–N curves. While more tests are needed, this tendency implies that the hardness and the stress level of the S–N curve are correlated, which is the usual observation in steel fatigue testing. For any number of cycles, the S–N curve of M-SKD11 was at least 20 pct higher in the stress amplitude over that of SKD11. As a comparison, the fatigue data for AISI 4340 steel, similarly tested,[28] is also shown in Figure 8. In the low-cycle fatigue region, the two tool steels have substantially higher fatigue resistance. The S–N curve for 4340 has a less steep slope than in the tool steels, and gradually approaches the fatigue limit of 550 MPa.

A fracture surface examination was performed in order to identify the origin of fatigue fracture. Fatigue crack initiation sites varied depending on the magnitude of applied alternating stress. Three types of fracture morphology were observed and are presented in Figure 9. When the stress was high, fatigue fracture initiated from the surface of the M-SKD11 specimens and one or more primary carbide particles were always found at the origin of fracture. This is shown in Figures 9(a) and (b). When the stress amplitude was reduced, a crack initiated near the surface, but from the interior, and spread toward the outer surface. Primary carbide particles were again found to fracture at the initiation site, as shown in Figures 9(c) and (d). In the case of SKD11 steel, however, both of these two types occurred at stresses above 1100 MPa. When the stress amplitude was lower than 1100 MPa, the fracture initiation site was the so-called fish-eye type, shown in Figures 9(e) and (f). This type contained fractured carbide particles in the center, from which a round region of smooth fracture surface developed. Figure 10 presents an example of matching micrographs of the center of a fish-eye and X-ray line analysis of C and Cr for an M-SKD11 sample. This sample, tempered at 793 K, failed at 8.4×10^3 cycles under the stress amplitude of 1525 MPa. It is clear that the fracture occurred only after the development of a fish-eye because the internally initiated and grown crack did not touch the specimen surface. It is not certain, however, whether the fracture of a large primary carbide particle is a precondition of the formation of the observed fish-eye, although this is commonly assumed to be the trigger of the fatigue fracture. The type of crack initiation for each data point on the S–N curves for both steels is also shown in Figure 8. In M-SKD11, surface initiation sites were confined to stress amplitudes higher than 1800 MPa, while the fish-eye type was observed for the fatigue life of more than 10^3 cycles. One sample between these two types exhibited near-surface crack initiation. On the other hand, in SKD11, the initiation sites at middle and high stress ranges were either at the surface or the near-surface sites. The fish-eye type was observed for the fatigue life of more than 2×10^4 cycles with the stress amplitude of 1100 MPa or lower.

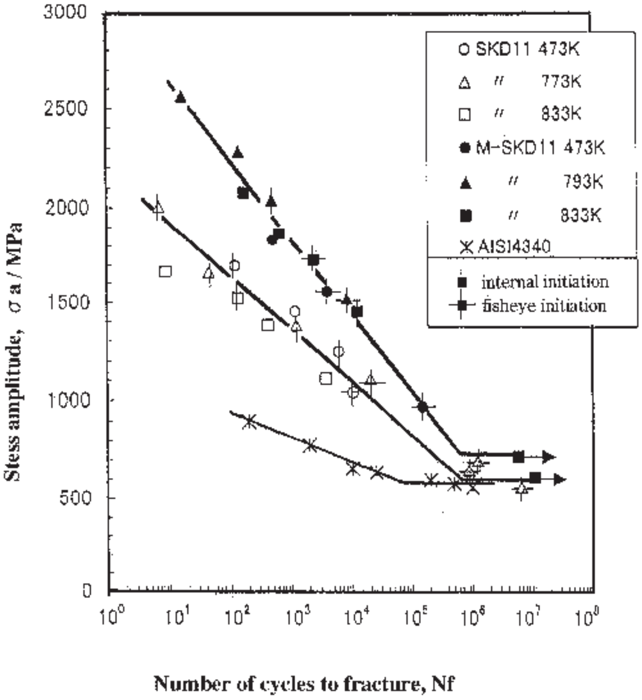

Fig. 8—S–N curves of steels tempered at 473, 773, 793, and 833 K. Data for 4340 steel similarly tested are also shown. Vertical line and cross-line superimposed on the symbols show the fatigue initiation sites with the exception of the surface.

The fish-eye fatigue initiation is commonly known to occur under high-cycle fatigue (above 10^6 cycles) of high-strength steels.[29] In these cases, the inclusion(s) at the center of the fish-eye is oxides, silicates, and sulfides. A limited number of cases with carbide-initiated fish-eyes are also reported.[30,31] The present results, showing over 100 times lower numbers of cycles when the fish-eye fracture is found, are the consequence of primary carbides. A similar observation of fish-eye fracture below 10^5 cycles has been reported in quenched and tempered high-speed tool steels (SKH51; 0.8C-4Cr-6W-5Mo-1.8V-0.5Co) that have the strength comparable to SKD11.[31] The initiation sites were nonmetallic inclusions of 63-μm average size. These samples had Vickers hardness values of 615 to 654. While it is not always known why fish-eye fracture develops at a given level of cycling in a certain material, Murakami *et al.*[29,32,33] have shown that the fatigue limit (σ_f) is empirically correlated to the hardness (HV) and the projected area of the initiating defect or flaw (A_d) existing at the surface as

$$\sigma_f = 1.41\,(\mathrm{HV} + 120)\,(A_d)^{-1/12} \qquad [1]$$

or the equation below when the flaw exists inside

$$\sigma_f = 1.56\,(\mathrm{HV} + 120)\,(A_d)^{-1/12} \qquad [2]$$

These equations are capable of predicting the fatigue limit in more than 20 different steels.

The relationship between the stress amplitude and maximum size of carbide particles at the fracture origin is presented in Figure 11. In both steels, as the stress amplitude decreases, the particle size of observed carbides has a tendency to increase. It was also noted that, when stress amplitude is high, a fatigue crack nucleates at a small carbide at the surface or

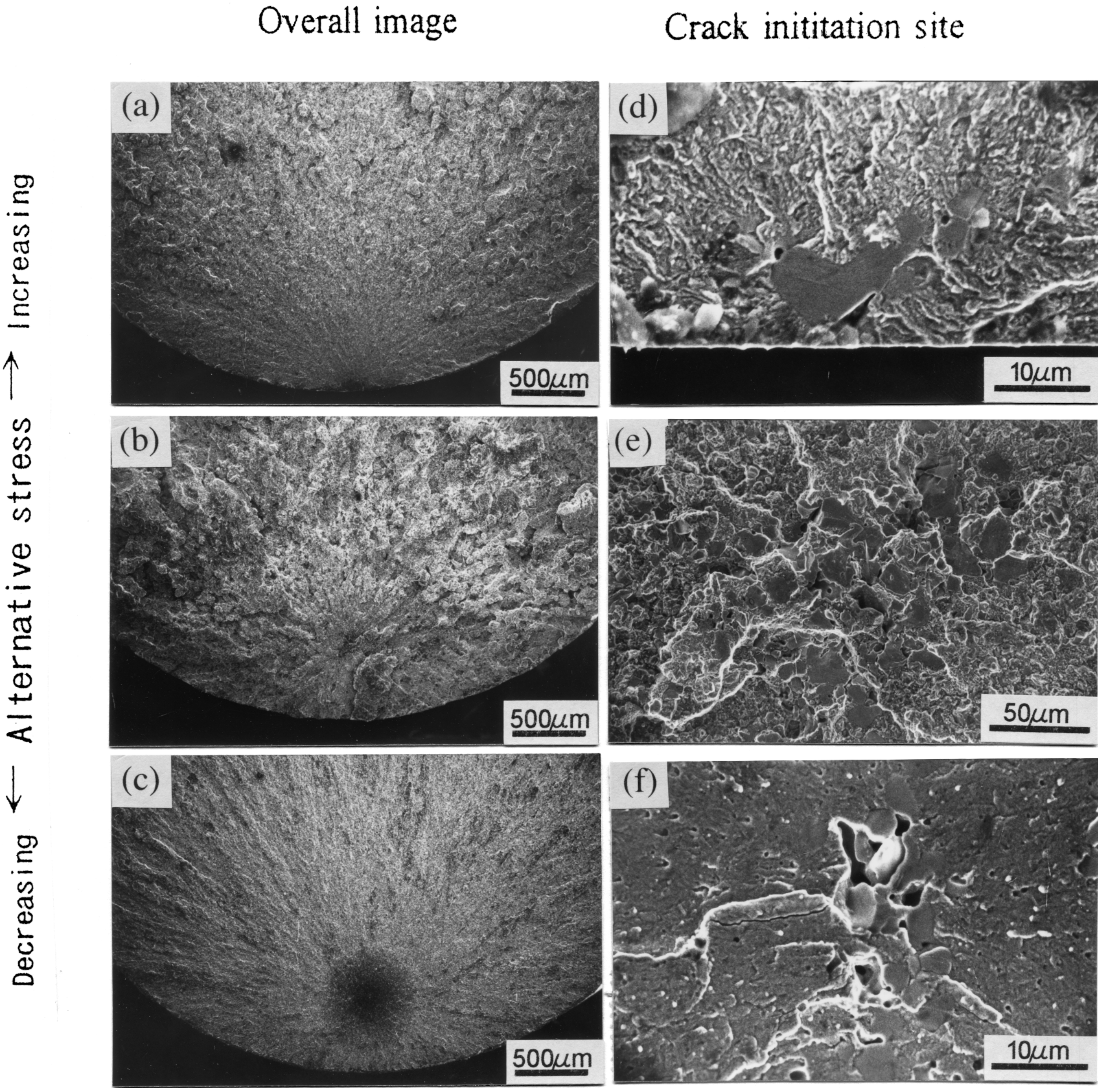

Fig. 9—Fatigue fracture surfaces classified according to the magnitude of applied cyclic stress: (*a*) and (*d*) M-SKD11, tempered at 473 K, $\sigma_a = 2149$ MPa, $N_f = 4.1 \times 10^1$ cycles. (*b*) and (*e*) SKD11, tempered at 473 K, $\sigma_a = 1698$ MPa, $N_f = 1.2 \times 10^2$ cycles. (*c*) and (*f*) M-SKD11, tempered at 473 K, $\sigma_a = 970$ MPa, $N_f = 1.5 \times 10^5$ cycles.

near surface and grows into a semi-circular (or truncated circular) crack. On the other hand, when stress amplitude is lower than a critical value, a fatigue crack nucleates at a large carbide particle in the interior and expands into a circular crack, producing fish-eye type fracture. In both cases, a carbide particle is present at the initiation site of the fatigue crack, and in almost all instances, carbides are fractured. In M-SKD11, the critical stress for surface to fish-eye fracture transition is 1800 MPa and is 1100 MPa for SKD11.

The minimum stress needed for surface or fish-eye induced fatigue fracture for SKD11 and M-SKD11 is calculated from the empirical Eq. [1] or [2] and is plotted in Figure 11 as open and filled triangles. The value of σ_f is 750 to 930 MPa for M-SKD11 and is 630 to 900 MPa for SKD11. These predicted values are lower than the observed fatigue stress amplitude. Furthermore, the lowest values (630 MPa for SKD11 and 750 MPa for M-SKD11) are in good agreement with the fatigue limits on the S–N curves shown in Figure 8. Note also that two samples that did not fail had the stress amplitude below the calculated fatigue limit.

When the sample fails during fatigue from a fish-eye, near surface, or surface site, the nominal value of the threshold stress intensity factor range (K_{fth}) can be estimated from the flaw size and the peak stress. The value of K_{fth} was obtained using the well-known formula for a circular interior crack and for a semicircular surface crack;[26] *i.e.,*

$$K_{\text{fth}} = Y(2/\pi)\,\sigma\sqrt{\pi c} \qquad [3]$$

where c is the radius of the crack equal to the radius of carbide existing in the center of the fish-eye. Here, $Y = 1$ for the inner crack or 1.12 for the surface crack. As a result, the mean values of K_{fth} are 3.7 MPa$\sqrt{\text{m}}$ for M-SKD11 and

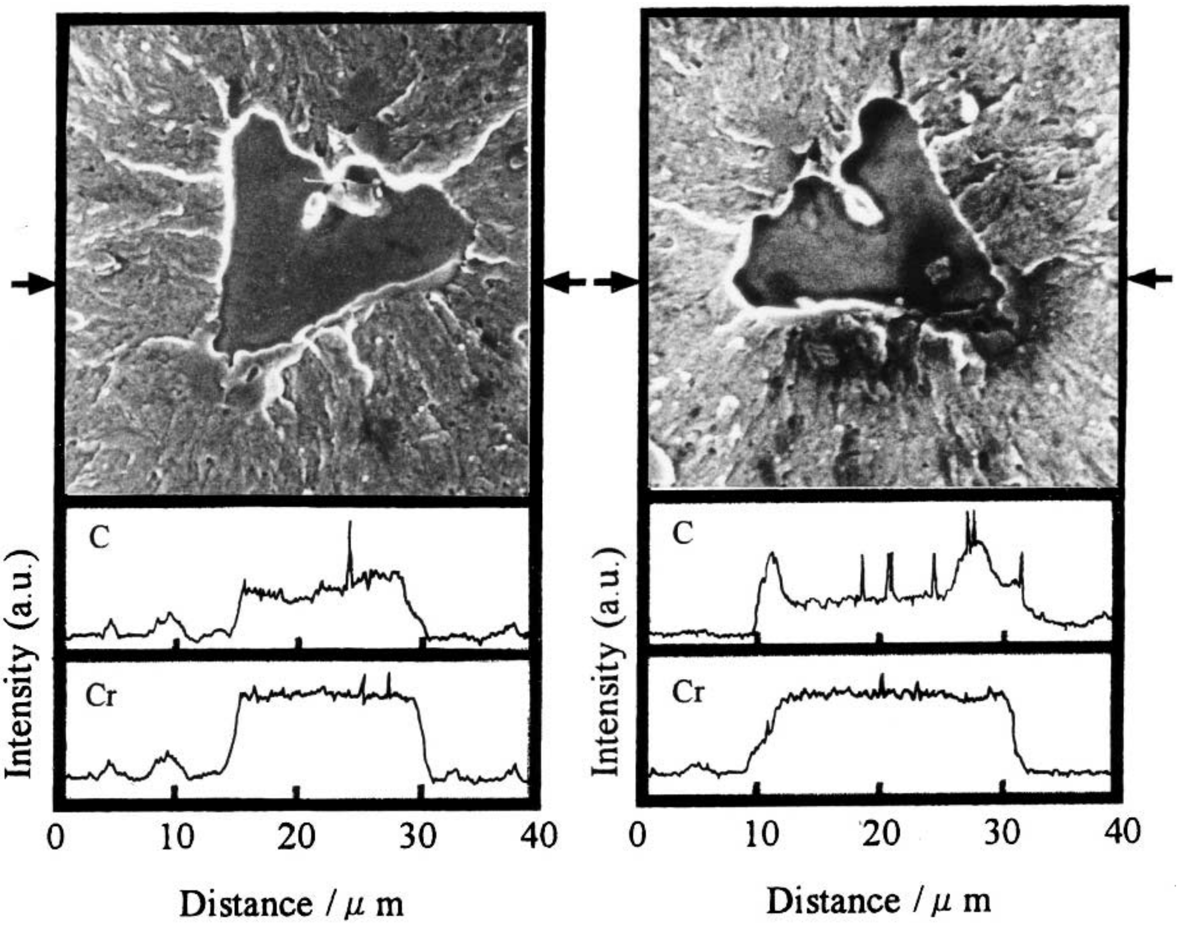

Fig. 10—Matching fractographs of M-SKD11 fatigued specimen tempered at 793 K, and X-ray line analysis of C and Cr. Applied alternating stress is 1525 MPa, and number of cycles to fracture is 8.4×10^3.

Table IV. Calculated Values of K_{IC} from the Size of Observed Crack

Steels	Tempering Temperature (K)	Stress Amplitude (MPa)	Number of Cycles to Fracture (N_f)	Diameter of Fish-Eye (μm)	Fatigue Fracture Toughness (MPa$\sqrt{\text{m}}$)
SKD11	473	867	6.8×10^4	39.5	12
	773	1110	2.1×10^4	152.2	15
M-SKD11	473	1560	4.0×10^3	152.7	22
	473	970	1.5×10^5	157.6	14
	793	1525	8.4×10^3	147.3	21
	833	1733	2.4×10^3	142.4	24
	833	1455	1.3×10^4	157.8	20

3.3 MPa$\sqrt{\text{m}}$ for SKD11. As a reference, a curved line is shown in Figure 11, which represents the relationship between the maximum size of carbide in the center of the fish-eye and the amplitude of stress when we assume that K_{fth} is 3.5 MPa$\sqrt{\text{m}}$, and approximate the lower bound of the observed fatigue strength. The K_{fth} value was raised by 12 pct in M-SKD11. These values are lower than that of the value in quenched-and-tempered 300 M containing 0.4C-0.8Cr-1.8Ni-0.4Mo-0.1V steel.[32] However, considering the high hardness in SKD11, these values are found reasonable. The value of K_{IC} also can be calculated from Eq. [3]. In this case, c is the radius of the fish-eye. The results are summarized in Table IV. The values of K_{Ic} ranged from 12 to 15 MPa$\sqrt{\text{m}}$ for SKD11 and 14 to 24 MPa$\sqrt{\text{m}}$ for M-SKD11. For the corresponding heat-treatment condition, M-SKD11 had 40 to 50 pct higher values of K_{Ic}.

For a given flaw size, the surface flaw has a higher stress intensity factor. This contributes to the surface fracture initiation, when many small flaws exist and a critical crack develops from one of them. This appears to be the case for M-SKD11 at high stresses. However, the number of potential sites for surface fracture is always less than that for possible internal fracture sites in tension-compression fatigue. This arises due to a large volume subjected to the applied maximum stress. This seems to contribute to the observation of both surface and near-surface fracture sites in SKD11 at higher stresses.

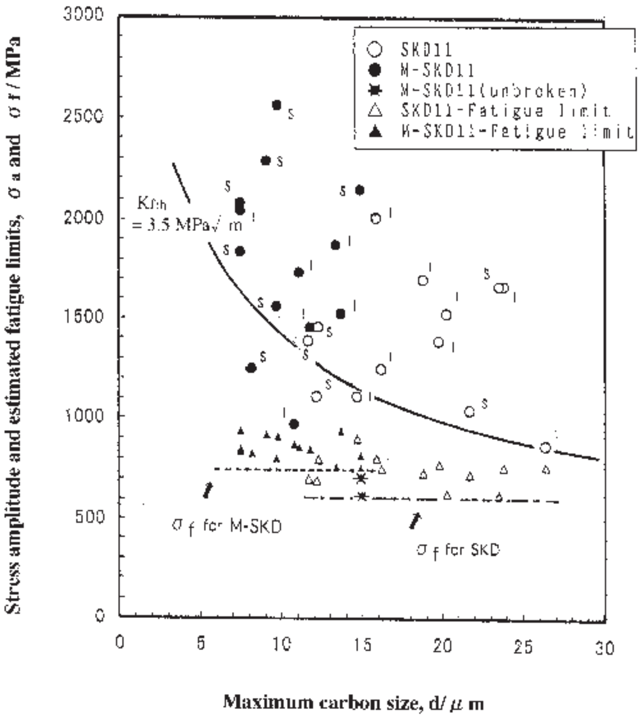

Fig. 11—Relation between applied cyclic stress and maximum particle size of M_7C_3 carbide existing at the root of fracture. Triangles show the estimated fatigue limits depending on the Murakami's equation, which are calculated from Eqs. [1] and [2], based on the hardness and carbide size. Two data points (*) represent no fracture. Subscripts S and I represent the fatigue initiation site at the surface or the interior of the specimen, respectively.

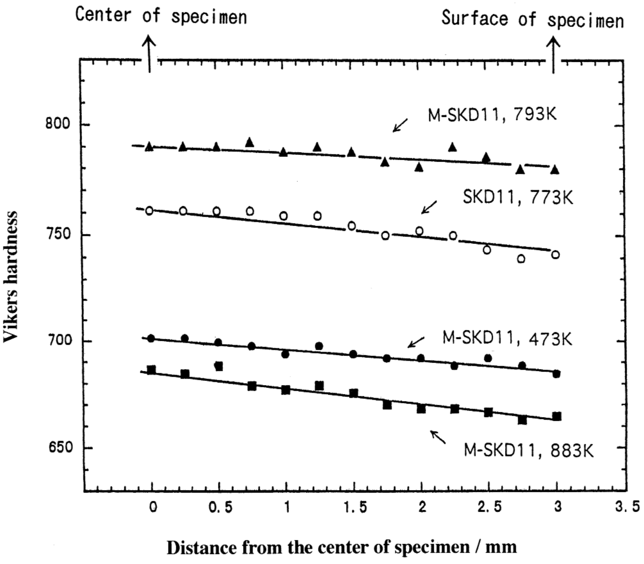

Fig. 12—The distribution of hardness from the center of the specimen toward the surface.

It has been suggested that the reason for internal fracture at low stress amplitude can be explained (1) by the tensile residual stress being induced during grinding and polishing or by cooling treatment from tempering temperature[35,36] and (2) by heterogeneous distribution of carbides in the specimen. Figure 12 shows the change in hardness measured from the center toward the surface in the radial direction of the specimens. The hardness decreases slightly (~20 HV) from the center toward the surface. The high hardness toward the center portion can be due to the differences in carbide concentration. In fact, the area fraction of the carbide inside is 30 to 40 pct larger than that at the surface. It is often reported that compressive stresses of several hundred Mega Pascals in magnitude are produced near the surface by lapping or heat treatment. However, the stress decreases abruptly toward the interior beyond tens of microns of depth. This means that a tensile residual stress exists at the somewhat deeper position considering the balance of force. However, the distance from the surface to the center of the fish-eye is more than hundreds of microns so that the influence of residual stress is considered unlikely. Note that post-temper cooling was done by air cooling, so it is unlikely to generate any significant residual stress.

Eventually, it appears that the greater the number of carbides present in the interior, the more likely that a crack will initiate from any of these carbides at a low stress range, although the static stress for carbide cracking, whose stress is much higher than that for fatigue, will be shown in Section D. In fact, there is one interesting fact in that many smaller fish-eyes can be observed on the same fatigue fracture surface. The reasons why carbides are easily broken at low stress should be clarified in order to further improve fatigue property.

As mentioned previously, the fatigue strength of M-SKD11 steel regulated the chemical compositions not to precipitate primary carbides is in a way superior to the SKD11 steel. The M-SKD11 steel has finer carbides and their volume fraction is small, so it is considered that the possibility of piling up of dislocations to the carbides decreases and the carbides are difficult to fracture. This is the reason for the higher fatigue strength of the M-SKD11.

C. *Cyclic Softening and Hardening Behavior*

Figure 13 shows the change of plastic strain during fatigue for both steels when an alternating stress near the yield strength is applied. Fatigue causes cyclic hardening or softening. Cyclic softening occurred for both tool steels tempered at 833 K, as the amount of cyclic strain increased with increasing cycle ratio. Cyclic hardening occurred for steels tempered at 473 K and at peak hardening temperatures. For the materials tempered at 833 K, plastic strain of SKD11 and M-SKD11 increased 205 and 63 pct, respectively. As for the materials tempered at 473 K, their plastic strain decreased 34 and 19 pct, respectively. The degree of cyclic softening and hardening of SKD11 is much larger than that of M-SKD11.

It is well known that cyclic hardening or softening depends on the value of the ratio of ultimate strength to yield strength (σ_B/σ_y) as an empirical law.[26] When this ratio is more than 1.4, the steel will cyclically soften, and when it is 1.2 or less, the steel will cyclically harden. When the value is in between 1.2 and 1.4, the steel remains unchanged. The σ_B/σ_y value of both steels tempered at 473 K is 1.4 to 1.5, and cyclic hardening is predicted. The ratio for steels tempered at 833 K is 1.2, which should result in cyclic softening. These trends agree with the empirical law, although the foundation for this law is obscure. For steels tempered at 733 or 793 K, the ratio is 1.3, and no cyclic hardening is predicted. However, the observed results suggest cyclic hardening.

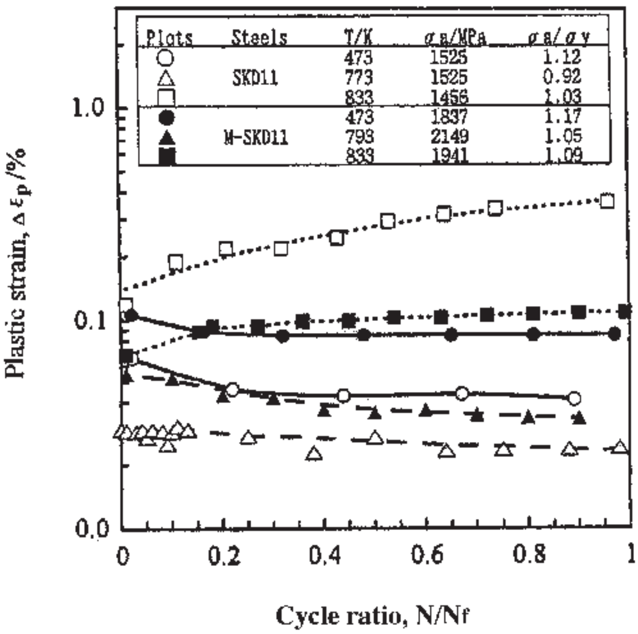

Fig. 13—Change of plastic strain during fatigue under stress-controlled condition for cold-work tool steels. σ_a—alternating stress, and σ_y—yield strength before and after fatigue testing.

Table V. Change of Volume Fraction (in Percent) of Retained Austenite*

Annealed	Temperature (K)	473	773	793	833
SKD11	before fatigue	19.7	7.3	0	0
	after fatigue	3.3	2.4	0	0
M-SKD11	before fatigue	13.5	—	4.4	0
	after fatigue	3.6	—	2.1	0

*Applied stresses are as follows: SKD11, 1525 MPa for 423 and 773 K tempered, 1456 MPa for 833 tempered. M-SKD11, 1827, 2149, and 1941 MPa for 473, 793, and 833 K tempered, respectively.

The observed softening in overpeak-tempered steels is understandable as the tempered martensite structure can be destabilized by strain localization processes, such as persistent slip bands and vein structure formation. The cyclic hardening of both steels in hardened conditions is surprising, since most martensitic structures tend to cyclic soften. It appears that this cyclic hardening behavior originates from the transformation of retained austenite to martensite, as presented in Table II. Table V shows the change in retained austenite content before and after cyclic loading. The applied stress amplitude for each steel was shown in Figure 12 and it was in the vicinity of the yield strength of each steel. Retained austenite was reduced to 2 to 4 pct during cyclic loading. The amount of the reduction (or transformation) for SKD11 was higher than that for M-SKD11. From this result, it is suggested that cyclic hardening results from the transformation of retained austenite to martensite during cyclic loading in the steels tempered at low or peak-hardening temperatures.

D. *AE Behavior*

To this point, we have discussed the relationship between fatigue strength and carbide cracking. However, it is important to know the stress required to break carbides. For the purpose of catching the breaking of carbides, it is effective to use an AE.

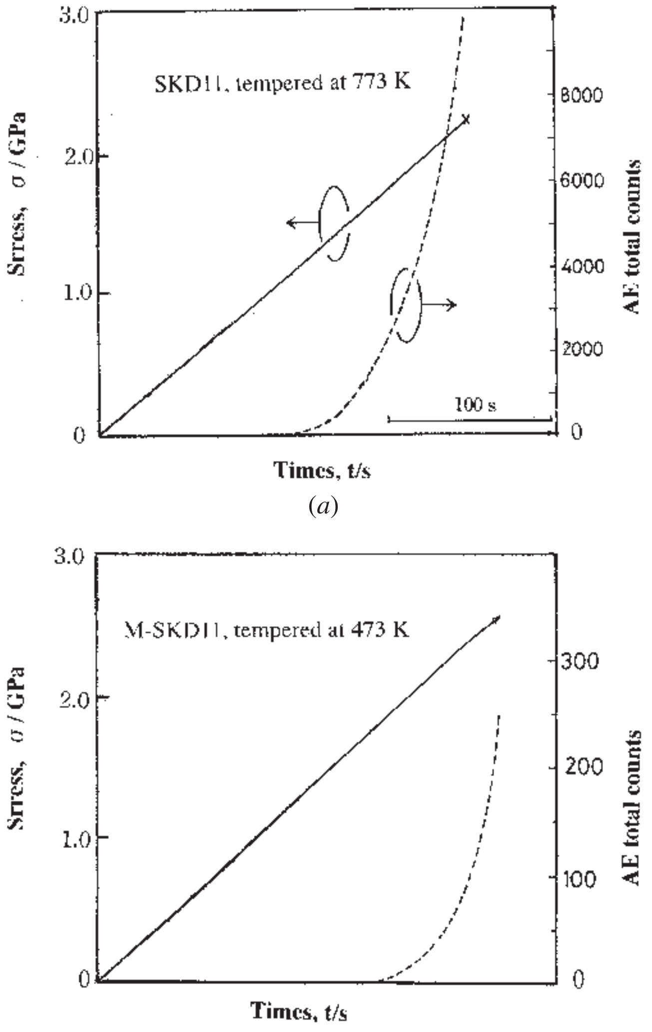

(*a*)

(*b*)

Fig. 14—Tensile and AE test results (*a*) for the SKD11 steel tempered at 773 K and (*b*) for the M-SKD11 steel tempered at 473 K during the first tensile loading. Solid lines represent the stress-time relation. Dashed lines represent the change of AE counts during tensile testing.

Both SKD11 and M-SKD11 samples were tested in tension using a two-channel AE detection system. The shape of the tensile specimen was an hourglass type with 5-mm minimum outer diameter. The crosshead speed was 4.2×10^{-3} mm/s. The AE signals obtained were discriminated on the basis of arrival-time difference of less than 5 μs, signifying that only these signals came from the center of the sample. Figure 14a shows the stress and cumulative AE event counts *vs* time of testing for an SKD11 sample and Fig. 14b for an M-SDK11. The peak amplitude of each AE signal was recorded and reported earlier.[24] Amplitude levels were quite low generally, even with high-sensitivity resonant AE sensors. The beginning of the AE observation (defined at the fifth event) occurs at 1.1 GPa for SKD11 and 1.8 GPa for M-SKD11, respectively. Note that these stress levels are much the same as those of the critical stress below which the fish-eye fracture was found (*i.e.,* 1.1 GPa for SKD11 and 1.8 GPa for

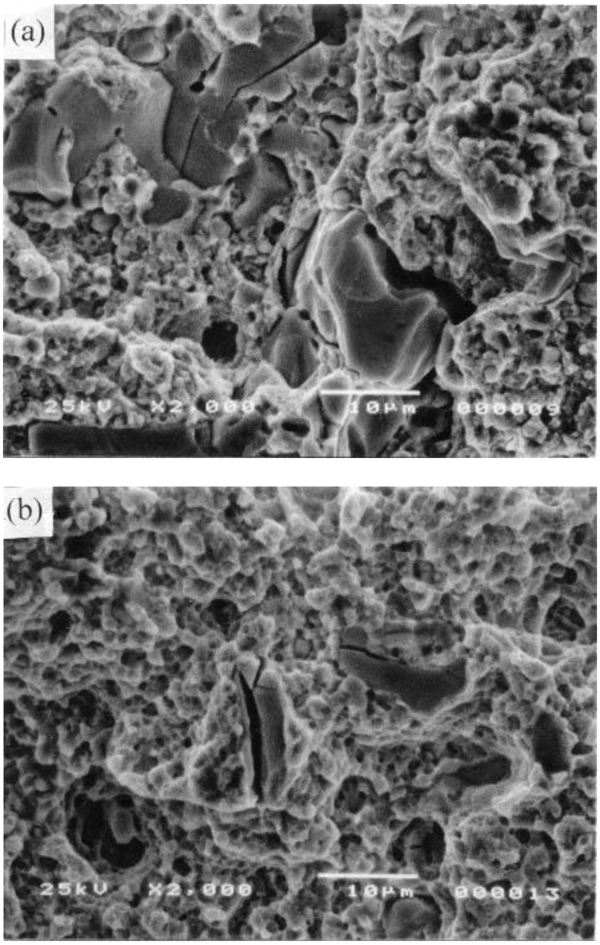

Fig. 15—Tensile fractured surfaces of (*a*) SKD11 tempered at 773 K and (*b*) M-SKD11 tempered at 473 K.

M-SKD11). It is considered that this finding results from the difference of carbide size involved for each steel. It is not clear why these stresses obtained by AE tests were in good agreement with the maximum stress for fracture with fish-eye, mentioned previously, or why these values were predicted to relate to an elastic breakdown. We could not find the definite correlation between them.

The AE behavior was similar in SKD11 samples, but the peak amplitude reached as high as 65 dB in SKD11 in comparison to the 43 dB limit in M-SKD11. This reflects larger and more numerous large carbides in SKD11. Detailed analysis of AE signal waveform has indicated that the observed AE signals result from a crack-opening type source of AE. This can be the cracking of a carbide particle as found in Figure 15. It can also be due to the separation of a carbide from the matrix or microcrack propagation. The latter mechanism was indicated as the AE source during load-hold at higher stresses (above 1.1 GPa in SKD11). At present, further source identification is not feasible from the signal analysis. However, it has been found that most carbide particles on the fracture surfaces are fractured. This indicates that the carbide cracking is the most plausible AE source.

The AE signals are considered to be from the cracking of carbide particles. This implies that low stress amplitude where no AE was observed and no carbide cracking occurred corresponds to the condition of fish-eye fracture. That is, a crack and an inclusion are equivalent in determining the fatigue limit. In other words, stress concentration is unimportant in initiating fatigue damage when the crack size falls below a limiting value.

IV. CONCLUSIONS

The fatigue behavior of a modified cold-work tool steel (M-SKD11) was investigated in connection with the microstructure and fracture surface morphology of the steel and was compared with that of SKD11. The main results are summarized as follows.

1. The S–N curve of M-SKD11 is at least 20 pct higher than that of SKD11, while K_{fth} values were raised by 12 pct in M-SKD11.
2. The fish-eye fracture initiation behavior was found above $\sim 10^4$ cycles.
3. The K_{Ic} values of M-SKD11 calculated from fish-eye size were 40 to 50 pct higher than those for SKD11.
4. The observed improvement originates from the refinement and volume reduction of primary carbides in M-SKD11.
5. Although a fractured carbide is usually found at the origin of a crack, AE analysis suggests that carbide fracture occurs only above 1.1 or 1.8 GPa in SKD11 or M-SKD11 under static tensile stressing.

ACKNOWLEDGMENTS

The authors thank Mr. K. Teramoto, Graduate Student, Himeji Institute of Technology, for his devotion in helping with this experiment, and the Machine and Engineering Workshop, Himeji Institute of Technology, for preparing many of the test pieces.

REFERENCES

1. F.A. Kivk: *Met. Technol.,* 1982, vol. 9, pp. 198-2024.
2. S. Inoue: *J. Jpn. Inst. Iron Steel,* 1987, vol. 73, pp. 1461-69.
3. T. Arakawa and M. Suzuki: *Bull. Jpn. Inst. Met.,* 1966, vol. 5, pp. 269-83.
4. N. Tsujii and G. Abe: *Sanyo Tech. Rep.,* 1995, vol. 2, pp. 77-83.
5. K. Ozaki, Y. Matsuda, and K. Sudoh: *CAMP-ISIJ, Jpn.,* 1994, vol. 7, p. 724.
6. J. Yoshida, M. Katsumata, and Y. Yamasaki: *CAMP-ISIJ, Jpn.,* 1991, vol. 4, p. 1896.
7. M. Knoe, K. Lange, and T. Altan: *J. Mater. Processing Technol.,* 1994, vol. 46, pp. 57-71.
8. K. Aramoti and G. Urano: *Bull. Jpn. Inst. Met.,* 1969, vol. 8, pp. 117-26.
9. K. Itoh, K. Sudou, Y. Tokiwa, and K. Matsuda: *J. Jpn. Elect. Furnace,* 1984, vol. 55, pp. 248-56.
10. T. Abe and K. Kanazawa: *J. Jpn. Soc. Mater. Sci.,* 1996, vol. 45, pp. 9-15.
11. N. Tsujii and G. Abe: *Sanyo Tech. Rep.,* 1994, vol. 1, p. 69.
12. J. Yoshida, M. Katsumata, and K. Kashiwagi: *CAMP-ISIJ, Jpn.,* 1992, vol. 5, p. 927.
13. N.M.A. Eid and P.F. Thomason: *Acta Metall.,* 1979, vol. 27, pp. 1239-49.
14. J. Lankford: *Engg. Fract. Mech.,* 1977, vol. 9, pp. 617-24.
15. Y. Murakami and M. Shimizu: *Trans. Jpn. Soc. Mech. Eng. A,* 1988, vol. 54, pp. 413-25.
16. H. Berns, J. Leng, W. Trojahn, R. Wahling, and H. Wisell: *Powder Metall. Int.,* 1987, vol. 19 (4), pp. 22-26.
17. J. Yoshida, M. Katsumata, and Y. Yamazaki: *J. Jpn. Inst. Iron Steel,* 1988, vol. 84, pp. 79-84.
18. Y. Natsume, K. Murakami, and T. Miyamoto: *Proc. Jpn. Soc. Mech. Eng.,* 1990, vol. 900 (86), pp. 323-25.

19. G. Abe, H. Nakamura, and H. Tyoh: *Bull. Jpn. Inst. Met.,* 1986, vol. 25, p. 438.
20. H. Sunada, K. Fukaura, K. Teramoto, N. Tsujii, and D. Yokoi: *Proc. 45th Meeting, Mater. Sci. Jpn.,* 1996, p. 149.
21. R.H.K. Honeycombe: *Steels—Microstructure and Properties,* Edward Arnold, London, 1990, pp. 156-60.
22. J. Durinin and K.A. Ridal: *J. Iron Steel Inst.,* 1968, Jan., pp. 60-67.
23. Anon: *Manual for X-Ray Diffraction*, 4th ed., Rigaku Denki Co., Tokyo, 1991, p. 56.
24. K. Fukaura and K. Ono: in *Progress in Acoustic Emission X,* T. Kishi *et al.,* eds., Japan Soc. for non-destructive Inspection, Tokyo, 2000, pp. 337-43.
25. P. Villars, A. Prince, and H. Okamoto: *Handbook of Ternary Alloy Phase Diagram,* ASM, Materials Park, OH, 1995, pp. 6632-33.
26. R.W. Hertzberg: *Deformation and Fracture Mechanics of Engineering Materials,* Wiley, New York, NY, 1989, p. 495.
27. *Metals Handbook,* 10th ed., Materials Park, OH, 2000, vol. 8, pp. 785-86.
28. S. Matsuoka, M. Yuyama, and B. Nishijima: *Trans. JSME,* 1986, vol. A52 (480), pp. 1831-38.
29. Y. Murakami: *Metal Fatigue: Effects of Small Defects and Nonmetallic Inclusions,* Yokendo Ltd., Tokyo, 1993, p. 78.90.106.
30. H. Berns: *Proc. Fatigue '87,* Charlottesville, VA, 1987, EMAS Ltd., London, 1987, vol. 1, pp. 527-36.
31. Y. Natsume, S. Miyagawa, Y. Uemura, and Y. Murakami: *J. Jpn. Inst. Mater. Sci.,* 1989, vol. 38 (10), pp. 1133-38.
32. Y. Murakami and T. Endo: *Int. J. Fatigue,* 1980, vol. 2 (1), pp. 23-30.
33. Y. Murakami, T. Ueda, and T. Nomoto: *Proc. Eur. Conf. on Fatigue,* Sept. 2000, Paper No. 069, pp. 1-8.
34. O. Vosikovsky: *Eng. Frac. Mech.,* 1979, vol. 11, pp. 595-602.
35. Y. Natsume, S. Miyagawa, and M. Muramatsu: *J. Jpn. Inst. Mater. Sci.,* 1988, vol. 37, pp. 606-11.
36. D. Yokoi: Sanyo Special Steel Co. Ltd., Hyogo, Japan, unpublished research, 1997.